Journal of Alloys and Compounds 517 (2012) 164–169

Contents lists available at SciVerse ScienceDirect

Journal of Alloys and Compounds

journal homepage: www.elsevier.com/locate/jallcom

Influence of processing methodology on the structural and magnetic behavior of $MgFe_2O_4$ nanopowders

J. Chandradass[a], Arvind H. Jadhav[a], Ki Hyeon Kim[b], Hern Kim[a,*]

[a] Energy and Environment Fusion Technology Center, Department of Environmental Engineering and Biotechnology, Myongji University, Yongin, Kyonggi-do 449-728, Republic of Korea
[b] Department of Physics, Yeungnam University, Gyeongsan, Gyeongsangbuk-do 712-749, Republic of Korea

ARTICLE INFO

Article history:
Received 18 September 2011
Received in revised form
15 December 2011
Accepted 15 December 2011
Available online 24 December 2011

Keywords:
Ceramics
Chemical synthesis
Characterization
Magnetic property

ABSTRACT

Three different wet chemistry routes namely reverse micelle, citrate gel and co-precipitation methods were used to synthesize magnesium ferrite nanopowders. The synthesized spinel was characterized by X-ray diffraction (XRD), Fourier transform infrared (FTIR), Raman spectroscopy techniques, transmission electron microscopy (TEM) and Superconducting Quantum Interference Device magnetometry (SQUID). The gel combustion method yield comparatively pure crystalline phase of $MgFe_2O_4$ and relatively higher saturation magnetization of 22.7 emu/g. The material synthesized using co-precipitation method yield other phases in addition to the targeted phase. The average diameter of nanoparticles obtained from reverse microemulsion route was about 19.6 ± 2 nm, and for those obtained from gel combustion and co-precipitation route are highly agglomerated. The reverse micelle process produces fine nanosized particles compared with other methods reported in the literature. Superconducting Quantum Interference Device (SQUID) magnetometer reveals that the ferrite nanopowders obtained from the reverse micelle, gel combustion and co-precipitation route exhibit superparamagnetism. The selection of $MgFe_2O_4$ synthesis method largely depends on the targeted applications and desired properties. The results reported in this study are useful for establishing a simple method for the preparation of $MgFe_2O_4$ nanopowders.

1. Introduction

Magnetic nanoparticles have been drawing much attention because they show unique features such as quantum size effect and magnetic tunneling. Magnesium ferrite is one of the important spinel widely reported for technological applications including high-density magnetic recording, hyperthermia [1,2], sensor [3–6] and anode material for lithium ion batteries [7]. In most of the envisaged applications, the particles perform best when the size of the nanoparticles is below a critical value, which is dependent on the material but is typically around 10–20 nm. Such individual nanoparticles have a large constant magnetic moment and behave like a giant paramagnetic atom with a fast response to applied magnetic fields with negligible remanence (residual magnetism) and coercivity (the field required to bring the magnetization to zero). These features make superparamagnetic nanoparticles very attractive for a broad range of biomedical applications [8,9]. It was reported that $MgFe_2O_4$ particles whose size was several μm have relatively high heat generation compared with other ferrites [10]. Therefore, it seems that $MgFe_2O_4$ nanoparticles with a precise size control have great capability for magnetic hyperthermia. The heating property in the AC magnetic field is strongly influenced by the particle size [11]. Therefore the present study is aimed at examining the effect of the synthesis route on the phase, particle size and magnetic properties. Three solution-based methods (co-precipitation, gel combustion and reverse micelle) were used for the preparation of $MgFe_2O_4$ nanopowders. Structural, morphological and magnetic properties were made by X-ray powder diffraction, Fourier transform infrared spectroscopy, Raman spectroscopy, transmission electron microscopy and Superconducting Quantum Interference Device (SQUID) magnetometer.

2. Experimental

2.1. Materials

Magnesium nitrate hexahydrate (Sigma–Aldrich), iron (III) nitrate nonhydrate (Aldrich), ammonium hydroxide (33%) (Sigma–Aldrich), citric acid monohydrate (Sigma–Aldrich), igepal CO-520 (Aldrich), heptane (Sigma–Aldrich) were used as reagents for synthesis.

2.2. Methods

2.2.1. Co-precipitation method

In the co-precipitation method, aqueous solutions of magnesium nitrate hexahydrate and iron (III) nitrate nonhydrate were dissolved in distilled water to a molar concentration of 1:2. The ammonium hydroxide was added to the precursor

* Corresponding author. Tel.: +82 31 330 6688; fax: +82 31 336 6336.
E-mail address: hernkim@mju.ac.kr (H. Kim).

0925-8388/$ – see front matter © 2011 Elsevier B.V. All rights reserved.
doi:10.1016/j.jallcom.2011.12.071

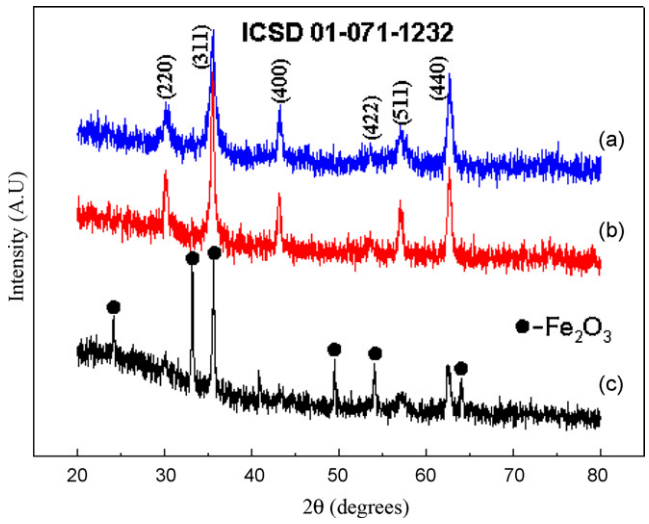

Fig. 1. XRD diffraction pattern for samples calcined at 600 °C from (a) reverse micelle; (b) gel combustion; (c) co-precipitation.

solution with constant stirring at room temperature. The final pH of the solution was maintained at 9. The obtained white precipitate was washed with ethanol to remove the unreacted molecules. Subsequently the precipitate was dried at 80 °C for 24 h and calcined at 600 °C for 2 h in air atmosphere.

2.2.2. Gel combustion method

In this technique, the magnesium nitrate hexahydrate and iron (III) nitrate nonhydrate were mixed together in aqueous medium to a molar concentration of 1:2. Citric acid was added to the mixed solution such that the molar ratio of citric acid to metal nitrate was unity (C/N = 1). The solution was continuously stirred for several hours and kept at the temperature of 60 °C until it turned into a brownish sol. The stabilized nitrate–citrate sol was rapidly heated to 80 °C. Viscosity and color changed as the sol turned into a transparent sticky gel. The gel was heat treated at 200 °C for 2 h and a fluffy, polymeric citrate precursor was gained. Finally, the prepared precursor was ground to a fine powder and calcined at 600 °C for 2 h.

2.2.3. Reverse micelle method

For the reverse micelle route, a tertiary system of heptane/Igepal CO 520/H_2O was selected. The required amount of magnesium nitrate hexahydrate and iron (III) nitrate nonhydrate salts were dissolved in distilled water to a molar concentration of 1:2. Heptane was used as organic solvent. The microemulsion solution was prepared by mixing 80 ml of poly(oxyethylene) nonylphenyl ether (a nonionic surfactant, Igepal CO-520), 200 ml of heptane and 39 ml of mixed aqueous salt solution. The microemulsion was mixed rapidly, and after 5 min of equilibration, 18 ml of NH_4OH was injected into the microemulsion. The precipitate was subjected to several cycles of washing with ethanol followed by centrifugation and finally dried in oven at 80 °C for 24 h. The dried powder was crushed in a mortar pestle and calcined at 600 °C for 2 h.

2.3. Characterization

The powder X-ray diffraction (XRD) patterns were recorded on a PANalytical X'pert MPD diffractometer. The morphology of the calcined powder was analyzed with a transmission electron microscopy (JEOL-3010) operating at an accelerating voltage of 300 kV. The average size of the particle estimated from the TEM micrograph using standard software (IMAGE J). Fourier transform infrared (FTIR) spectra were acquired with a JASCO FT/IR-6300 spectrometer. FTIR spectra of the powders were measured on pellets prepared by mixing the powder with KBr. Raman spectra were measured at room temperature with a JASCO NRS-3300 spectrometer. A 532 nm Ar ion laser was used as the excitation source and its power was kept at 10.5 mW. The magnetic properties of calcined powder samples were investigated using a SQUID magnetometer (Quantum design, MPMS XL-7).

3. Results and discussion

3.1. Structural and morphological analysis

Fig. 1a and b depicts the X-ray diffractographs of $MgFe_2O_4$ ferrite nanocrystals by reverse microemulsion and gel combustion routes, respectively. The peak position and relative intensity of all diffraction peaks observed for both samples matched well with standard

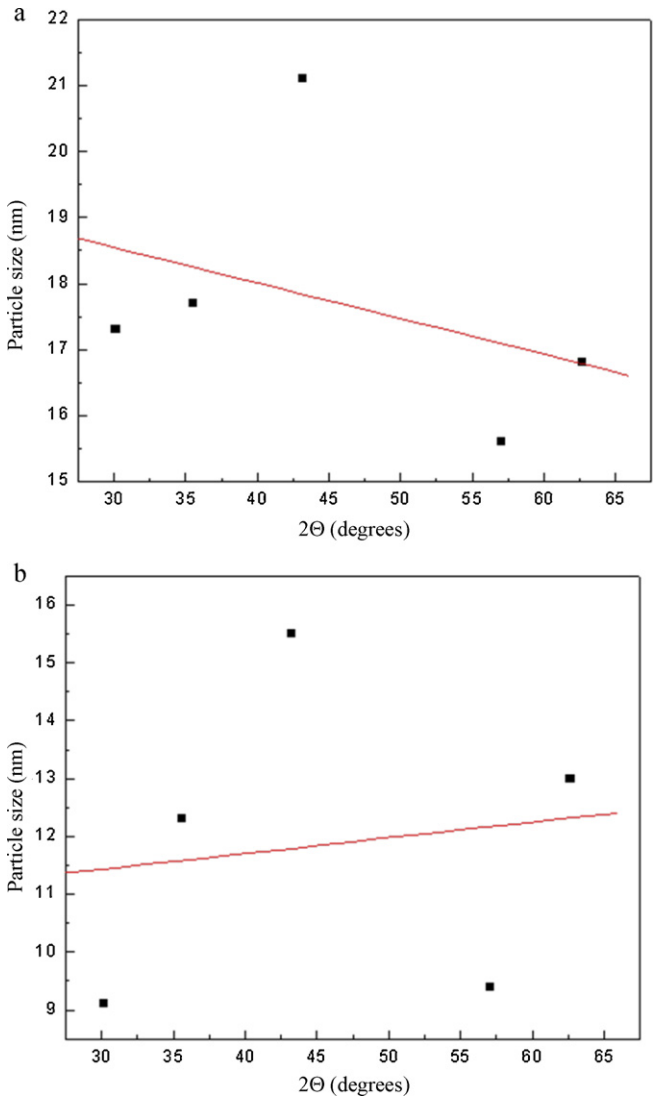

Fig. 2. Plot of peak position vs. crystallite size (a) combustion and (b) reverse micelle.

powder diffraction data (ICSD 01-071-1232). The diffraction peaks at 2θ values of 30.1°, 35.6°, 43.2°, 53.6°, 57°, and 62.6° could be ascribed to Bragg reflections of (2 2 0), (3 1 1), (4 0 0), (4 2 2), (5 1 1), and (4 4 0) planes which can be readily indexed to the spinel phase. No characteristic peaks of impurities were detected, confirming the formation of the cubic spinel structure of ferrite nanocrystals. The peak broadening of the diffraction pattern is mainly due to four factors: microstrains (deformation of the lattice), faulting (extended defects), crystalline domain size and domain size distribution [12]. If we assume that the samples are free of strains and faulting, the peak broadening is only due to the crystalline domain size [13]. According to the Debye–Scherrer formula, the average crystallite size can be estimated from the half-width of the most intense peak (3 1 1). Based on the diffraction peak positioned at different degrees, we estimate the crystallite size by plotting crystallite size vs. peak positions and extrapolation of the straight line by linearly fitting the points (Fig. 2). The crystallite size of samples prepared from combustion and reverse micelle method was 18.7 ± 2.2 nm and 11.34 ± 3 nm respectively. The difference in crystallite size was probably due to the different preparation conditions followed here which gave rise to different rates of ferrite formation, favoring the variation in crystallite size [14]. The nanocrystals obtained from the gel combustion method (Fig. 1b) shows the highest intensity, indicating their highest crystallinity

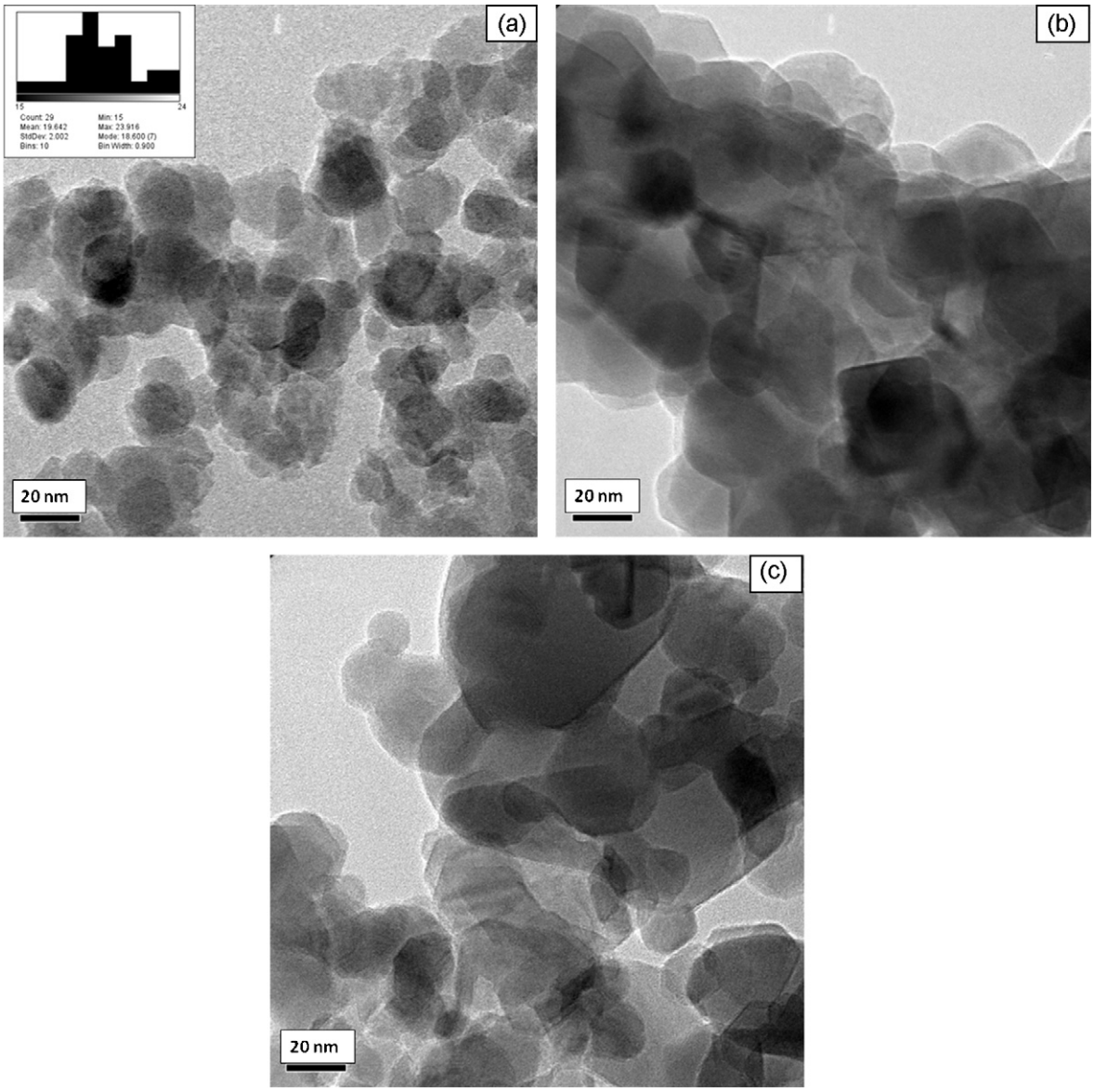

Fig. 3. TEM image of $MgFe_2O_4$ ferrite nanocrystals obtained from (a) reverse micelle (inset displays particle size distribution); (b) gel combustion; (c) co-precipitation method.

among all the synthesized nanocrystals. The X-ray diffractograph of nanocrystals obtained from the chemical co-precipitation method (Fig. 1c) shows sharp and weak diffraction peaks corresponding to crystalline Fe_2O_3 and spinel ferrite component. Thus it can be concluded to a greater extent, the phase formation are determined by preparation methods.

Fig. 3 depicts TEM micrographs of nanocrystals obtained from reverse micelle, gel combustion and co-precipitation methods. Inset at the top left corner in Fig. 3a shows the particle size distribution of nanocrystals prepared from reverse micelle method. The digitized image was imported into the program, IMAGE J and the populations of particles with respect to mean particle diameter were determined. 29 particles were measured from TEM micrograph to establish particle size distribution histograms. The histogram was created using IMAGE J with binning widths of 0.9 nm. The mean size and standard deviation resulted from IMAGE J were 19.6 nm and 2 nm, respectively. However, the gel combustion and co-precipitation method (Fig. 3b and c) produces highly agglomerated particles. The particle size determined by TEM in the present work is compared with other methods reported in the literature (Table 1). Among all the chemical processes that were developed for the preparation of $MgFe_2O_4$, the reverse micelle process reported in this study produces fine nanosized particles.

3.2. Spectral analysis

Typical FTIR spectra of nanocrystals obtained from reverse microemulsion, gel combustion and chemical co-precipitation routes are shown in Fig. 4. The spectra presented are of the crystals calcined at 600 °C for 2 h. The FTIR spectra of nanocrystals exhibit peaks around 3440 and 1630 cm^{-1} attributed to the stretching vibrations of hydrogen-bonded surface water molecules and hydroxyl groups [15]. The peak near 1600 cm^{-1} could be ascribed to in plane O—H bending of adsorbed water [16]. The peak around 2351 (reverse micelle), 2320 cm^{-1} (gel combustion) and 2363 cm^{-1} (co-precipitation) is typical of CO_2 absorption. The nanocrystals obtained from the reverse microemulsion and gel combustion method exhibit peak at 1050 cm^{-1} attributed to the C—O stretching vibration typical of C—OH groups for example of an ester or alcohol. The peak around 1382 cm^{-1} for nanocrystals prepared from reverse micelle is typical of CH_3 bending modes. The presence of OH vibration and CO_2 absorption band after calcination are due to

Table 1
Comparison of particle size determined from TEM.

Methods	Particle size (TEM) (nm)	Crystallite size (nm)	References
Hydrothermal	20	20	[33]
Ball milling	Not mentioned	19–72	[34]
Co-precipitation	37	26	[6]
Combustion (glycine fuel)	30–38	Not mentioned	[4]
Solution synthesis	Not mentioned	84	[3]
Polymer precursor	Not mentioned	100	[35]
Sol–gel method	Not mentioned	35	[36]
Aging process	40–50	Not mentioned	[37]
Reverse co-precipitation	30	15	[38]
Combustion (citric acid)	Not mentioned	17.8	[39]
Reverse micelle	39	31	[40]
Reverse micelle	19.6 ± 2 nm	12.3	Present work

the moisture absorption from atmosphere. In ferrites, metal ions are situated in two different sub lattices, designated as tetrahedral and octahedral according to the geometrical configuration of the oxygen nearest neighbors. The higher frequency band ν_1, around 600 cm^{-1}, is attributed to the intrinsic vibration of the tetrahedral sites, and the low frequency band ν_1 around 475 cm^{-1} is ascribed to the intrinsic vibration of the octahedral sites, thus confirming that samples prepared are spinel in structure [17,18].

Room temperature Raman spectra of samples were recorded in the range of 100–1150 cm^{-1}, as shown in Fig. 5. The Raman features are assigned to the vibrational modes from the nanoparticles crystalline structure. Raman features other than those related to the spinel phase ($MgFe_2O_4$) were not observed for the sample synthesized from reverse micelle and gel combustion method. $MgFe_2O_4$ spinel has a cubic structure belonging to the space group Fd3 m. Although the full unit cell contains 56 atoms ($Z = 8$), the smallest bravais cell contains 14 atoms ($Z = 2$). As a result, the factor group analysis predicts the following modes in $MgFe_2O_4$ spinel [10]:

$$A_{1g}(R) + E_g(R) + F_{1g} + 3F_{2g}(R) + 2A_{2u} + 2E_u + 4F_{1u}(IR) + 2F_{2u}$$

There are five Raman active modes ($A_{1g} + E_g + 3F_{2g}$), which are all observed at ambient condition in this present study. Wang et al. [19] found a Raman mode at 646 cm^{-1} attributed to order disorder effect. Contradict to this Nakagomi et al. [20] suggest that the Raman mode peaking at 670 cm^{-1} was due to the substitution of the Fe ions by Mg ions in the tetrahedral sites and not associated to order–disorder effect. They claimed that the large mass difference between the two ions (Fe^{3+} and Mg^{2+}) splits the A_{1g} mode into two branches; the lightest ion (Mg^{2+}) corresponds to the Raman mode peaking at 715 cm^{-1} whereas the heaviest ion (Fe^{3+}) accounts for the presence of the Raman mode peaking at 670 cm^{-1}. Kreisel et al. have reported that the cubic ferrites containing tetrahedral $Fe^{3+}O_4$ are characterized by a strong A_{1g} Raman band in the 660–720 cm^{-1} region, reflecting the local lattice effect in the tetrahedral sub lattice, whereas the Raman modes observed in the lowest frequency region (460–640 cm^{-1}) predominated by the stretching vibration associated to the octahedral $Fe^{3+}O_6$ sub lattice [21]. Despite the previously mentioned disagreement all authors agree that the highest-frequency Raman modes are associated to the tetrahedral sublattice. However in the present study, the peak at 707 cm^{-1} assigned to A_{1g} mode of $MgFe_2O_4$. Fig. 5 also shows the Raman spectrum of samples prepared from co-precipitation. The peak at 227 and 503 cm^{-1} were assigned to A_{1g} modes and those at 247, 293, 412 and 612 cm^{-1} were assigned to E_g modes of α-Fe_2O_3 [22]. The other peak at 661 cm^{-1} was assigned to γ-Fe_2O_3 as reported elsewhere [23].

3.3. Magnetic properties

Fig. 6 shows the magnetization versus applied field curve for ferrite samples. The *M–H* hysteresis loops indicating superparamagnetic property at a temperature of 300 K for $MgFe_2O_4$ ferrite nanocrystals synthesized via reverse microemulsion is presented in Fig. 5a. The absence of hysteresis, remanence, and coercivity at 300 K are indicative of the presence of superparamagnetic and single domain crystals. The value of magnetization for $MgFe_2O_4$ ferrite nanocrystals obtained from reverse microemulsion was

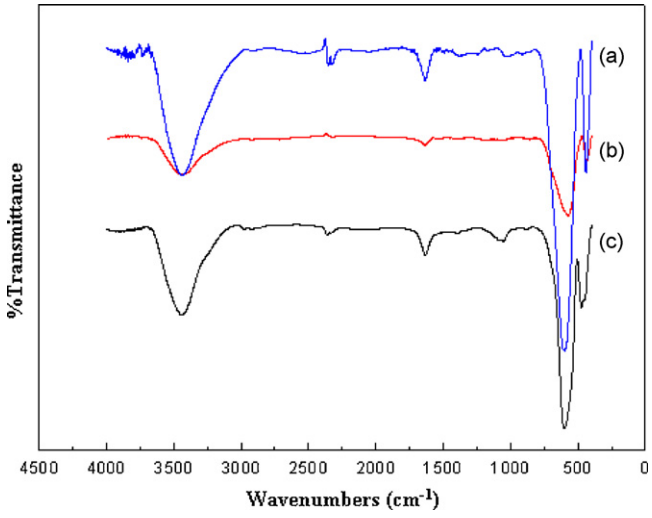

Fig. 4. Fourier transform infrared spectra of the powders produced by (a) reverse micelle; (b) gel combustion; (c) co-precipitation.

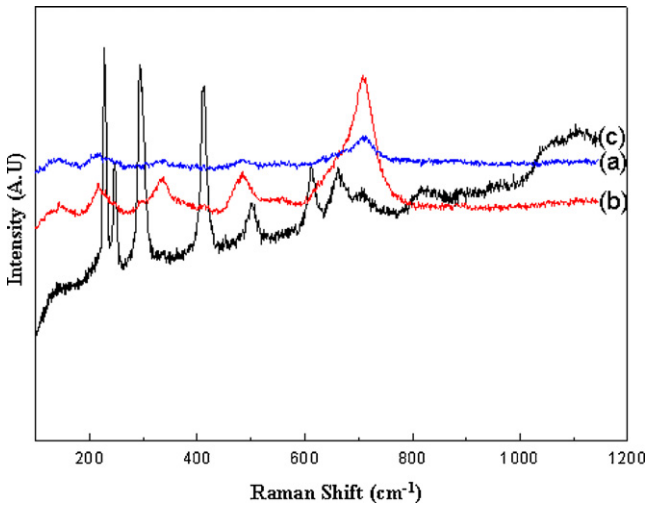

Fig. 5. Raman spectra of the powders produced by (a) reverse micelle; (b) gel combustion; (c) co-precipitation.

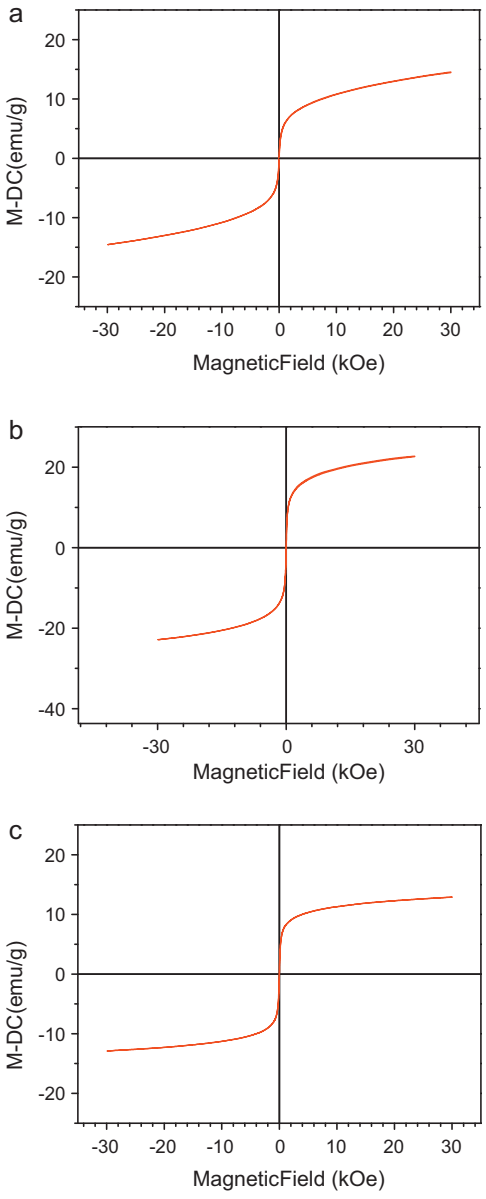

Fig. 6. Magnetization curves of $MgFe_2O_4$ ferrite nanocrystals obtained from (a) reverse micelle; (b) gel combustion method; (c) co-precipitation.

14.5 emu/g. On the other hand, the magnetic saturation values for the corresponding crystals obtained via gel combustion and co-precipitation methods were found to be 22.7 and 12.9 emu/g, respectively. It is well-known that the magnetic properties of nanocrystals are predominantly dictated by the intrinsic properties of materials such as the anisotropy and saturation magnetization. Surface effects can lead to a decrease of the magnetization for oxide nanoparticles, with respect to the bulk value. This reduction has been associated with different mechanisms, such as the existence of a magnetically dead layer on the particle's surface or the existence of spin-glass like behavior of the surface spins [24]. The existence of some degree of spin canting in the whole volume of the particle, in addition to the disordered surface layer, could be an alternative explanation of this additional decrease of the saturation magnetization. It should be mentioned that similar evolution in the magnetization with the particle size has been found in γ-Fe_2O_3 [25] and mixed ferrite [14] nanocrystals prepared from micelles. The non-ferromagnetic phase present in sample prepared from co-precipitation method results in reduction of saturation magnetization [26].

The magnetic behavior of nanocrystals has a marked dependence on the decrease in particle size, where the surface effects start to dominate. Nanocrystals with a large surface/volume ratio show enhanced spin disorder relative to large crystals when measured with the same values of applied field and temperature [27]. The surface layer magnetic moment anomalies may be due to broken exchange bonds, a high anisotropy layer on the surface, or a loss of the long-range order in the surface layer. These effects are more intense in the case of ferrites because of the super exchange interactions through the oxygen ions [28]. The relatively higher saturation values for $MgFe_2O_4$ ferrite nanocrystals obtained from the citrate gel method may be due to the fact that the anisotropic features of these nanocrystals have enhanced dipole–dipole interaction, favoring a head-to-tail orientation [29].

3.4. Implications of various methods

From XRD pattern, for co-precipitation it can be concluded that there are other phase in the sample. This may be due to the difference in precipitation of component elements, whereas the homogeneity of both the cation in the case of gel combustion and reverse micelle phase purity is relatively better [30]. Another aspect of using each of this method for synthesis of $MgFe_2O_4$ is energy requirement and degree of simplicity of the method. The most lengthy and energy intensive method is co-precipitation owing to requirement of long calcinations periods. Although co-precipitation is well known and most used method, due to its energy requirements may not be suitable method [30]. Gel combustion method although is the most widely used process for the synthesis of magnetic nanocrystals but leads to the aggregation of nanocrystals with a relatively broad size distribution, whereas nanocrystals prepared by the reverse micelle technique have well-defined boundaries and narrow size distribution [31,32]. The microreactors in reverse micelle not only control shape and size but also reduce the aggregation process of crystals because the surfactants could adsorb on the crystal surface when the crystal size approaches to that of the water pool. As a result, the crystals obtained via reverse micelle are generally very fine compared to those from other processes [32].

In view of the above, the selection of synthesis method for the $MgFe_2O_4$ depends on the desired phase purity, morphology, yield and energy requirement for the synthesis. Also based on targeted application synthesis method is used, for example in catalytic application porous morphology is preferred; hence gel combustion method need to be used. In hyperthermia application, the particles perform best when the size of the nanoparticles is below a critical value, typically around 10–20 nm. Therefore reverse micelle method needs to be used for hyperthermia application.

4. Conclusions

- The spinel $MgFe_2O_4$ was synthesized using three different synthesis methods namely co-precipitation, gel combustion and reverse micelle method.
- The study demonstrates that reverse microemulsion route gives a successful way for preparing $MgFe_2O_4$ ferrite nanocrystals with average diameter of 19.6 ± 2 nm. The synthetic procedure developed in the present study offers several advantageous features for the synthesis of magnetic nanocrystals. First, the synthetic process is economical and environmentally friendly, because it involves inexpensive and less toxic iron salts. Second, as the particle size is below the critical value, the coercivity and remanence become negligible, leading to a superparamagnetic state, which

could be characteristically described as a transformation from multidomain nature to single domain nature.

- As stated by Ma et al. [11], magnetic nanoparticles in the superparamagnetic regime have high heating efficiency even if their coercivity is equal or close to zero. The use of superparamagnetic nanoparticles also solves several problems associated with ferromagnetic heating agents i.e. no residual magnetization is left after the therapy and lower magnetic field are required for an effective and significant heating of the tissue. Furthermore, these studies provide an excellent superparamagnetic nanoparticulate system, which may be used as a heating agent for magnetic hyperthermia application.

Acknowledgments

This research work was supported by Basic Science Research Program (No. 2011-0027369) and by Priority Research Centers Program (No. 2011-0022968) through the National Research Foundation of Korea (NRF) funded by the Ministry of Education, Science and Technology.

References

[1] Y. Ichiyanagi, M. Kubota, S. Moritake, Y. Kanazawa, T. Yamada, T. Uehashi, J. Magn. Magn. Mater. 310 (2007) 2378.
[2] H. Hirazawa, H. Aona, T. Naohara, T. Maehara, M. Sato, Y. Watanabe, J. Magn. Magn. Mater. 323 (2011) 675.
[3] K. Mukherjee, D.C. Bharti, S.B. Majumder, Sens. Actuators B 146 (2010) 91.
[4] J.Y. Patil, M.S. Khandelkar, I.S. Mulla, S.S. Suryavanshi, Curr. Appl. Phys. (2011), doi:10.1016/j.cap.2011.06.029.
[5] S. Darshane, I.S. Mulla, Mater. Chem. Phys. 119 (2010) 319.
[6] P.P. Hankare, S.D. Jadhav, U.B. Sankpal, R.P. Patil, R. Sasikala, I.S. Mulla, J. Alloys Compd. 488 (2009) 270.
[7] N. Sivakumar, S.R.P. Gnanakan, K. Karthikeyan, S. Amaresh, W.S. Yoon, G.J. Park, Y.S. Lee, J. Alloys Compd. 509 (2011) 7038.
[8] A-H Lu, E.L. Salabas, F. Schuth, Angew. Chem. Int. Ed. 46 (2007) 1222.
[9] Q. Chen, Z. John Zhang, Appl. Phys. Lett. 73 (1998) 3156.
[10] T. Maehara, K. Konishi, T. Kamimori, H. Aono, H. Hirazawa, T. Naohara, S. Nomura, H. Kikkawa, Y.Watanabe, K. Kawachi, J. Mater. Sci. 40 (2005) 135.
[11] M. Ma, Y. Wu, J. Zhou, Y. Sun, Y. Zhang, N. Gu, J. Magn. Magn. Mater. 268 (2004) 33.
[12] Y.S. Fu, X.W. Du, A.Sergai, J. Liu, J. Am. Chem. Soc. 129 (2007) 16029.
[13] S. Bai, J. Hu, D. Li, R. Luo, A. Chen, C.C. Liu, J. Mater. Chem. 21 (2011) 12288.
[14] S. Kumar, V. Singh, S. Aggarwal, U.K. Mandal, R.K. Kotnala, J. Phys. Chem. C 114 (2010) 6272.
[15] L.A. Garcia-Cerda, S.M. Montemayor, J. Magn. Magn. Mater. 294 (2005) e43.
[16] G. Vaidyanathan, S. Sendhilnathan, R. Arulmurugan, J. Magn. Magn. Mater. 313 (2007) 293.
[17] Y. Ahn, E.J. Choi, E.H. Kim, Rev. Adv. Mater. Sci. 5 (2003) 477.
[18] N. Wu, L. Fu, M. Su, M. Aslam, K.C. Wong, V.P. Dravid, Nano Lett. 4 (2004) 383.
[19] Z. Wang, P. Lazor, S.K. Saxena, H.St.C. O'Neil, Mater. Res. Bull. 37 (2002) 1589.
[20] F. Nakagomi, S.W. Da Silva, V.K. Garg, A.C. Oliveira, P.C. Morais, A. Franco Jr., J. Solid State Chem. 182 (2009) 2423.
[21] J. Kreisel, G. Lucazeau, H. Vincent, J. Solid State Chem. 137 (1998) 127.
[22] Y.-S. Cho, Y.-D. Huh, Bull. Korean Chem. Soc. 30 (2009) 1413.
[23] M.I. Baraton, G. Busca, V. Lorenzelli, R.J. Willey, J. Mater. Sci. Lett. 13 (1994) 275.
[24] R.H. Kodama, J. Magn. Magn. Mater. 200 (1999) 359.
[25] N. Feltin, M.P. Pileni, Langmuir 13 (1997) 3927.
[26] P. Xu, X. Han, M. Wang, J. Phys. Chem. C 111 (2007) 5866.
[27] E. Hasmonay, J. Depeyrot, M.H. Sousa, F.A. Tourinho, J.C. Bacri, R. Perzynski, Y.L. Raikher, I.J. Rosenman, Appl. Phys. 88 (2000) 6628.
[28] R.D.K. Misra, A. Kale, R.S. Srivastava, O. Senkov, Mater. Sci. Technol. 19 (2003) 826.
[29] D. Yu, X. Sun, J. Zou, Z. Wang, F. Wang, K.J. Tang, J. Phys. Chem. B 110 (2006) 21667.
[30] P.V. Gosavi, R.B. Biniwale, Mater. Chem. Phys. 119 (2010) 324.
[31] M.P. Pileni, in: J.H. Fendler (Ed.), Nanocrystals and Nanostructured Films, Wiley-VCH, Weinheim, 1997.
[32] Y. Li, C.W. Park, Langmuir 15 (1999) 952.
[33] T. Sasakia, S. Oharaa, T. Nakaa, J. Vejpravovab, V. Sechovskyb, M. Umetsua, S. Takamia, B. Jeyadevanc, T. Adschiria, J. Supercrit. Fluids 53 (2010) 92.
[34] N. Sivakumar, A. Narayanasamy, J.-M. Greneche, R. Murugaraj, Y.S. Lee, J. Alloys Compd. 504 (2010) 395.
[35] R.A. Candeia, M.A.F. Souza, M.I.B. Bernardi, S.C. Maestrelli, I.M.G. Santos, A.G. Souza, E. Longo, Mater. Res. Bull. 41 (2006) 183.
[36] A. Pradeep, P. Priyadharsini, G. Chandrasekaran, J. Magn. Magn. Mater. 320 (2008) 2774.
[37] Q. Xu, Y. Wei, Y. Liu, X. Ji, L. Yang, M. Gu, Solid State Sci. 11 (2009) 472.
[38] H. Aono, H. Hirazawa, T. Naohara, T. Maeha, Appl. Surf. Sci. 254 (2008) 2319.
[39] R. Sergiode Biasi, L. Helena Guimardes Cardaso, J. Brank de campos, D. Ruben sanchez, J. Batista marimom da cunha, Mater. Res. 12 (2009) 225.
[40] P. Holec, J. Plocek, D. Niznansky, J. Poltierova Vejpravov, J. Sol–Gel Sci. Technol. 51 (2009) 301.